Journal of Power Sources 185 (2008) 363–373

Contents lists available at ScienceDirect

Journal of Power Sources

journal homepage: www.elsevier.com/locate/jpowsour

Numerical characterization of a microscale solid-oxide fuel cell

Chen-li Sun*, Hsien-Chih Ou[1]

Department of Mechanical Engineering, National Taiwan University of Science and Technology, 43 Section 4 Keelung Road, Taipei 10607 Taiwan

ARTICLE INFO

Article history:
Received 1 April 2008
Received in revised form 14 June 2008
Accepted 16 June 2008
Available online 26 June 2008

Keywords:
Microscale solid-oxide fuel cell (μSOFC)
Performance analysis
Thermal management
Oxygen composition
Flow channel design

ABSTRACT

In this study, a single unit of planar micro-solid-oxide fuel cell (μSOFC) is investigated numerically to evaluate the influences of flow channel design, oxygen composition, and thermal operating conditions on cell performance. Four flow channel designs are examined under the co-flow configuration: serpentine, double serpentine, rod bundle, and oblique rib. For all designs, the contacts areas of interconnect to electrodes are kept consistent to maintain the ohmic losses at the same level. To characterize the mass transport effects, there are three different compositions, 100% O_2, 50% O_2/50% N_2 and air, fed to the cathode inlet. Different thermal conditions, adiabatic and isothermal, are applied to the outer boundary of the μSOFC and the results are compared. The outcomes suggest that both thermal conditions and oxidant composition show remarkable influences on μSOFC performance. Under adiabatic conditions, the rise of cell temperature causes a decrease in reversible voltage, deteriorating the overall cell competence. When oxygen is diluted with nitrogen, local gas diffusion becomes dominant to the cathode reaction. Bulk flow, on the other hand, plays a minor role in cell performance since there is little deviation in the polarization curves for all flow channel designs, even at high current densities. For comparison, the flow visualization technique is employed to observe the transport phenomena in various flow channel designs. The flow patterns are found to resemble the concentration distribution, providing a useful tool to design μSOFCs.

1. Introduction

Innovative approaches to portable power sources have attracted great attention due to their vital roles in consumer electronics and military applications. With the growing demands for longer lifetime and smaller sizes, conventional batteries are inadequate to fulfill these needs. As the MicroElectroMechanical Systems (MEMS) field flourishes, many researchers attempt to exploit microfabrication technologies to develop microscale power devices. Several concepts, such as microcombustion engines [1], micropneumatic energy conversion [2], and miniaturized fuel cells [3], have been explored to realize micro power generation. Among them, solid-oxide fuel cell (SOFC) has become a very promising approach because of its high generation efficiency and structural simplicity. As a result of its high operating temperature, SOFC does not require expensive precious metal catalysts, nor does it suffer from water management problems [4]. Hence, miniaturized SOFCs would be suitable for powering long-duration devices and remote-communication electronics.

Morse and Jankowski [5] are the pioneers of employing the microfabrication technique to reduce the size of SOFCs. Using silicon wafer as the support substrate, thin films of anode, electrolyte, and cathode materials are deposited to establish the freestanding membrane. An open circuit voltage of 0.8 V is measured at 316 °C for the thin-film solid-oxide fuel cells. Later, Jankowski et al. [3] proposed a manifold-supported structure which integrates the insulating layers, the heater, the electrodes, and the electrolyte layer into the micro-machined manifold. Using dilute fuel mixtures, the scaled-down fuel cell package is capable of delivering 0.15 W cm^{-2} of power output at an operating temperature of 600 °C.

Several concerns arise when designing thin-film SOFCs. Since thin-film structures are inevitably subjected to intrinsic and thermal stress, reliability issues become crucial. Srikar et al. [6] presented analytical models to study the effects of electrolyte thickness on electrochemical performance, structural stability, and thermal loss for micro-machined SOFCs. Their results indicate that cell performance is nearly independent of electrolyte thickness in the micron range when operating at 490–600 °C. Tang et al. [7] studied the effects of thin-film geometry on thermal-mechanical reliability of μSOFCs. A corrugated supported membrane for the thin circular electrolyte was proposed to reduce the structure stress. Moreover, Shao et al. [8] proposed a thermally self-sustained μSOFC configuration that utilizes the thermal energy released from oxidation reaction. Without auxiliary heating, the fuel cell stack

* Corresponding author. Tel.: +886 2 2737 6452; fax: +886 2 2737 6460.
E-mail address: clsun@mail.ntust.edu.tw (C.-l. Sun).
[1] Present address: Delta Electronics, 31-1 Xingbang Road, Guishan Industrial Zone, Taoyuan County, 33370 Taiwan.

0378-7753/$ – see front matter © 2008 Elsevier B.V. All rights reserved.
doi:10.1016/j.jpowsour.2008.06.048

Nomenclature

a'	stoichiometric coefficient of the electrochemical reaction
A	total current collection area
c_p	specific heat
D	effective mass diffusion coefficient
E	operating voltage
F	Faraday constant
h	enthalpy
i	charge flux
i_{av}	average current density
i_0	exchange current density
i_T	transfer current
J	diffusion flux
k	thermal conductivity
$\dot{m}$	mass flow rate
M	molecular weight
P	pressure
ΔP	pressure drop in interconnect
R	gas constant
T	temperature
U	velocity vector
$\dot{W}$	power
x	x-coordinate
y	y-coordinate
Y	species mass fraction
z	z-coordinate

Greek symbols

α	transfer coefficient
β	concentration exponent
ε	porosity
ϕ	electrical potential
γ	tortuosity
η	overpotential
κ	permeability
μ	viscosity
ρ	density
σ	electrical conductivity
$\boldsymbol{\tau}$	shear stress tensor

Subscript

a	anode
act	activation
av	average
c	cathode
conc	concentration
eff	effective
f	fluid
flow	flow
i	species i
inlet	inlet of interconnect
ohm	ohmic
outlet	outlet of interconnect
preheat	preheat
s	solid

is successfully maintained at 500–600 °C and a power output of 350 mW is obtained at 1.0 V.

Although μSOFC is emerging as a potential candidate for microscale power generation, several problems remain unaddressed. Since heat conduction and mass diffusion become the dominant mechanisms in microscale transport, reduction in size might lead to thermal management difficulties and diffusion limitations. To further comprehend the physical consequences of downscaling SOFC, numerical investigation is carried out for four flow channel designs in this study. Pure hydrogen is supplied to the anode, while three different compositions of oxidant, 100% O_2, 50% O_2/50% N_2 and air, are fed to the cathode to examine the effects of mass transport. There are two types of thermal boundary conditions imposed: isothermal and adiabatic. To evaluate the μSOFC performances, polarization curves, as well as the distributions of species concentrations and temperature are compared. Moreover, silicon-based microchannels are fabricated and the flow visualization technique is implemented experimentally to obtain flow patterns that help understand the transport phenomena in the four flow channel designs of interconnects.

2. Model construction

2.1. Assumptions

The software package CFD-ACE+ [9], which adopts the finite volume approach, is employed to perform the cell-level simulations of μSOFC. In this study, the following assumptions are made:

1. The fuel cell is under stationary operation.
2. The reactant gases obey ideal gas behaviors.
3. The flow field is laminar.
4. The physical properties of all materials are isotropic and homogenous.
5. The effects of gravity are negligible.

2.2. Mathematical models

To simulate the physical phenomena in SOFC, CFD-ACE+ employs a set of differential equations governing the transport of mass, momentum, energy, and charge.

Continuity equation:

$$\frac{\partial(\varepsilon\rho)}{\partial t} + \nabla\cdot(\varepsilon\rho\mathbf{U}) = 0 \tag{1}$$

Conservation of momentum:

$$\frac{\partial(\varepsilon\rho\mathbf{U})}{\partial t} + \nabla\cdot(\varepsilon\rho\mathbf{U}\mathbf{U}) = -\varepsilon\nabla P + \nabla\cdot(\varepsilon\boldsymbol{\tau}) + \frac{\varepsilon^2\mu\mathbf{U}}{\kappa} \tag{2}$$

Conservation of species:

$$\frac{\partial(\varepsilon\rho Y_i)}{\partial t} + \nabla\cdot(\varepsilon\rho\mathbf{U}Y_i) = \nabla\cdot\mathbf{J}_i + M_i a_i' \frac{i_T}{F} \tag{3}$$

Conservation of energy:

$$\frac{\partial(\varepsilon\rho h)}{\partial t} + \nabla\cdot(\varepsilon\rho\mathbf{U}h) = \nabla\cdot\left(k_{\text{eff}}\nabla T + \sum_i \mathbf{J}_i h_i\right) + \varepsilon\boldsymbol{\tau} : \nabla\mathbf{U} + \varepsilon\frac{\partial P}{\partial t} + i_T(\phi_s - \phi_f) + \sigma(\nabla\phi)^2 \tag{4}$$

Conservation of charge:

$$\nabla\cdot\boldsymbol{i}_s = -\nabla\cdot\boldsymbol{i}_f = \nabla\cdot(-\sigma_s\nabla\phi_s) = -\nabla\cdot(-\sigma_f\nabla\phi_f) = i_T \tag{5}$$

In the species conservation equation, the diffusion flux $\mathbf{J}_i$ is modeled by Fick's Law, $\mathbf{J}_i = \rho D_{i,\text{eff}}\nabla Y_i$. The effective mass diffusion coefficient $D_{i,\text{eff}}$ is acquired from the Bruggman model, $D_{i,\text{eff}} = \varepsilon^\gamma D_i$.

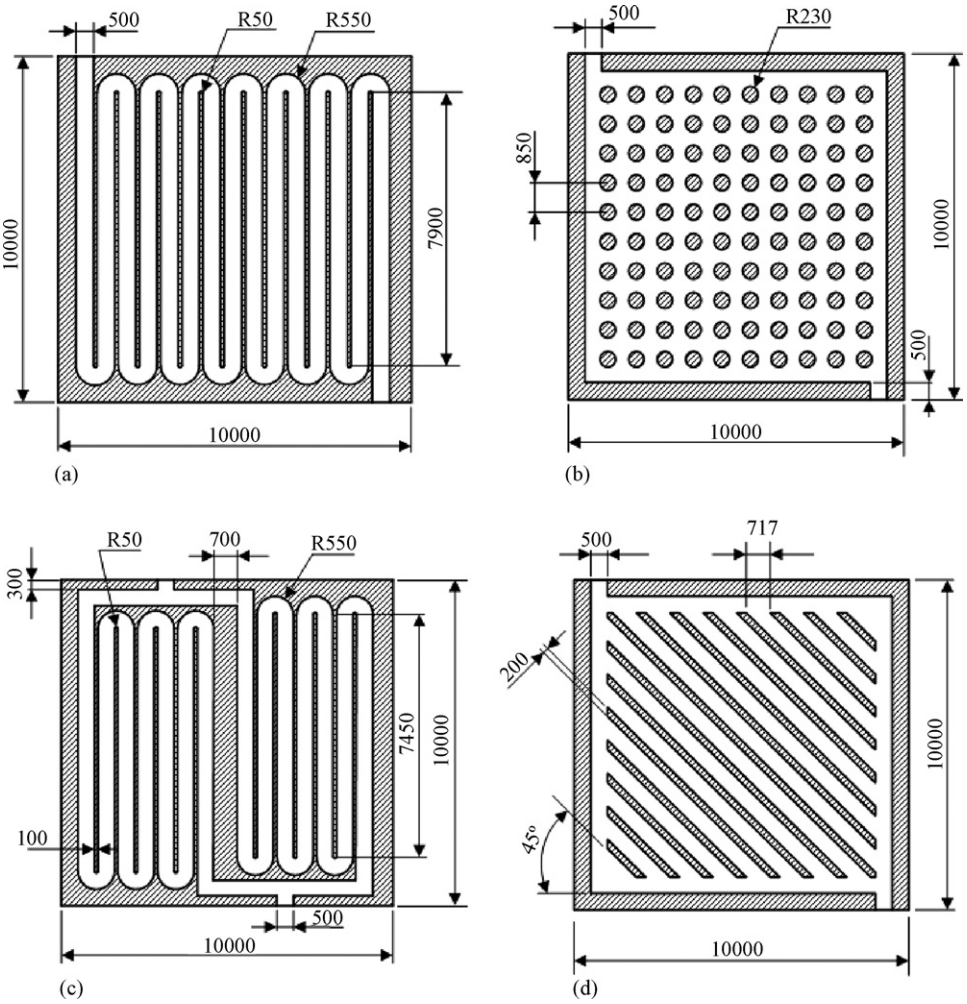

Fig. 1. The four flow channel designs investigated in this study: (a) serpentine, (b) rod bundle, (c) double serpentine and (d) oblique rib, unit: μm.

In the energy conservation equation, effective thermal conductivity k_{eff} is used to account for the porosity effects in electrodes:

$$k_{\text{eff}} = -2k_{\text{s}} + \left[\frac{\varepsilon}{2k_{\text{s}} + k_{\text{f}}} + \frac{1-\varepsilon}{3k_{\text{s}}}\right]^{-1} \tag{6}$$

Moreover, the conversion of chemical energy to thermal energy is specified in the enthalpy flux term $\sum_i \mathbf{J}_i h_i$. For μSOFC, there are two heat sources: Joule heating and heat production associated with active and concentration losses. In Eq. (4), $\sigma(\nabla\phi)^2$ represents the Joule heating effects, which occurs in all solid regions such as electrodes, electrolyte, and interconnects. Whereas, the heat generation caused by active and concentration losses is considered to take place in the PEN (positive/electrolyte/negative) region, and is represented by $i_T(\phi_{\text{s}} - \phi_{\text{f}})$. For the electrochemical reaction, a modified form of the Butler–Volmer equation is used:

$$i_T = i_0 \left\{ \exp\left[\frac{\alpha_{\text{a}} F}{\text{RT}}(\phi_{\text{s}} - \phi_{\text{f}})\right] - \exp\left[\frac{-\alpha_{\text{c}} F}{\text{RT}}(\phi_{\text{s}} - \phi_{\text{f}})\right] \right\} \prod_{i=1} Y_i^{\beta_i} \tag{7}$$

By setting the operating condition, the aforementioned models are solved to predict the local electrical, thermal, and mass transfer profiles. To obtain the polarization curve, average current density is evaluated by integrating the local current density at the area of the current collector.

$$i_{\text{av}} = \frac{1}{A} \int_A \mathbf{i}_{\text{s}} \cdot \text{d}\mathbf{A} \tag{8}$$

The aforementioned mathematical models contain adjustable parameters that can be set by calibration. As described in Ramakrishna et al. [10], the adjustable parameters are determined by comparing the computational results to available polarization curves of a single-cell SOFC under a range of fuel and oxidant compositions.

2.3. Model geometry

The simulation domain is a single unit of μSOFC which consists of anode, electrolyte, cathode and two interconnects. The footprint area of μSOFC is 1 cm × 1 cm, and the thickness of the interconnect which bears the flow channel is 1 mm. To improve the mechanical reliability, a conventional electrolyte-supported structure is carried out instead of following the thin-film approach. The thickness of the electrolyte is 200 μm, while both the anode and the cathode have thicknesses of 50 μm. There are four different flow channel designs examined: serpentine, double serpentine, rod bundle, and oblique rib, as shown in Fig. 1. The depth of the flow channel is fixed at 500 μm. For the serpentine and double serpentine designs, the channel is 500 μm wide with bends that have a 300 μm radius of curvature. The rod bundle design comprises a square array of 10 columns. The diameter of the columns is 460 μm and the pitch is 850 μm. In the oblique rib design, the ribs are 200 μm wide with an interval of 507 μm, while the angle of the rib alignment toward the inflow is 45°. Among the four different designs, the variation

Table 1
Physical properties of μSOFC model

Component	Electrolyte	Anode	Cathode	Interconnect
Material	YSZ	Ni/ZrO_2	LSM	$LaCrO_3$
Electrical conductivity ($S\,m^{-1}$)	0.01	10^5	7700	100
Porosity (%)	1	45	44	–
Permeability (m^2)	10^{-18}	10^{-12}	10^{-12}	–
Thermal conductivity ($W\,m^{-1}\,K^{-1}$)	2.7	6	11	2.11
Average pore size (μm)	0.3	1.6	2.74	–
Density ($kg\,m^{-3}$)	–	–	–	6770
Specific heat ($J\,kg^{-1}\,K^{-1}$)	–	–	–	550.5

of ohmic overpotential is minimized by keeping the contact areas of interconnects and electrodes at 33.1–36.6% of the active area so that the individual contributions of mass transport can be clarified.

Table 1 summarizes the physical properties used in the simulations. The ionic conductivity of electrolyte is set to $10\,S\,m^{-1}$. Hence, the corresponding ohmic resistances for anode, cathode, and electrolyte are 5×10^{-6}, 6.5×10^{-5}, and $0.2\,\Omega$, respectively. For all flow channel designs, the ohmic resistance of an interconnect is approximately $0.2\,\Omega$. On each electrode, the electrochemical reactions are expressed as

$$\text{Anode}: \quad 2H_2 + 2O^{2-} \rightarrow 2H_2O + 4e^-$$

$$\text{Cathode}: \quad O_2 + 4e^- \rightarrow 2O^{2-}$$

2.4. Boundary conditions

Pure hydrogen is supplied to the anode inlet with a mass flow rate of $10^{-8}\,kg\,s^{-1}$, while three different compositions of reactant, pure O_2, 50% O_2/50% N_2 and air, are fed to the cathode inlet. The flow configuration and coordinates of the model are illustrated in Fig. 2. For oxygen and air, the mass flow rate at the cathode inlet is fixed at $8 \times 10^{-8}\,kg\,s^{-1}$. For 50% O_2/50% N_2, the mass flow rate is determined by stoichiometry and is equivalent to $1.6 \times 10^{-7}\,kg\,s^{-1}$. The temperature of the reactants is set to 1073 K for both inlets and far-field boundary conditions are applied to the outlets. The voltage potentials on the surfaces of the current collectors are given to exhibit the external load, and the lateral walls of the μSOFC are electrically insulated. To study the influences of thermal management, two types of thermal boundary conditions are assumed: isothermal and adiabatic. Under isothermal condition, the wall temperature is fixed at 1073 K. Under adiabatic conditions, the generated heat can only be carried away by convection of the reactants. This is similar to the thermal environment in which a cell unit operates within a stack assembly or a single cell wrapped in perfect insulation operates alone. Table 2 lists the cell operating conditions and the inlet Reynolds numbers in this study. Since the corresponding Reynolds numbers are smaller than 10 in the interconnects, the laminar flow hypothesis is validated.

2.5. Model discretization

Grid studies are performed to determine the optimal strategy for mesh generation. Two main types of grid are tested: structured and mixed grid, which contains structured and prismatic unstructured meshes. The results of the grid sensitivity test are depicted in Fig. 3 with average grid size spanning from 3×10^{-4} to $2.6 \times 10^{-3}\,mm^3$. It is found that lower sensitivity of grid size to current density is achieved when structured grid is implemented to serpentine, double serpentine, and rod bundle designs. For the oblique rib design, sharp corners exist in the flow passage. The mixed grid demonstrates better robustness and is therefore used for the oblique rib design. The schematic drawing of the grid is shown in Fig. 4. To save computational time and retain reasonable accuracy, mesh numbers are maintained between 359,058 and 537,138 so that the average grid size is approximately $5.1 \times 10^{-4}\,mm^3$. When the minimum reduction in residuals for each variable is less than 10^{-4}, the computations quit the iterative procedure.

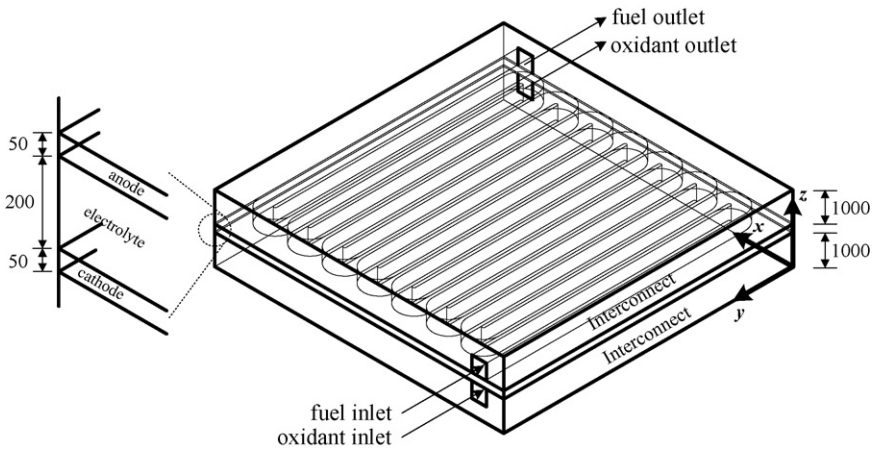

Fig. 2. Flow configuration, unit: μm.

Table 2
The cell operating conditions and the Reynolds numbers at inlets

Anode			Cathode			Thermal boundary
Fuel	$\dot{m}_a$ ($kg\,s^{-1}$)	Re_a	Oxidant	$\dot{m}_c$ ($kg\,s^{-1}$)	Re_c	
H_2	10^{-8}	0.92	O_2	8×10^{-8}	3.09	Isothermal
H_2	10^{-8}	0.6–0.9	O_2	8×10^{-8}	1.9–3.1	Adiabatic
H_2	10^{-8}	0.92	50% O_2/50% N_2	1.6×10^{-7}	6.7	Isothermal
H_2	10^{-8}	0.92	Air	8×10^{-8}	3.67	Isothermal

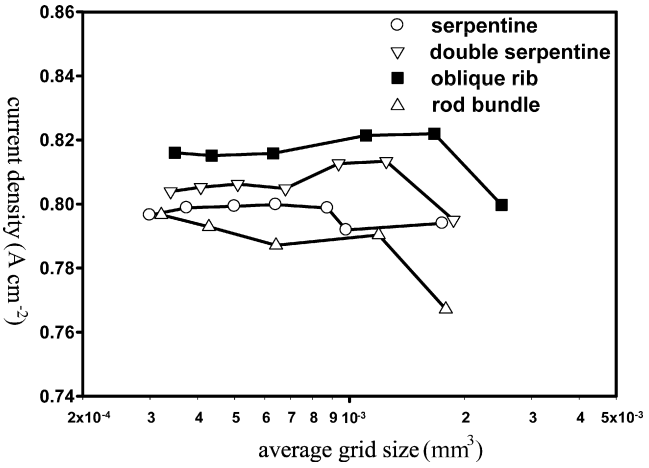

Fig. 3. Grid study for μSOFC model, open symbols denote structured grid, while solid symbols denote mixed grid. Isothermal condition, $E = 0.28$ V, and pure oxygen is used.

3. Results and discussion

3.1. Influences of thermal boundary conditions

Fig. 5 shows the comparison of cell characteristics under different thermal boundary conditions for μSOFC. From Fig. 5(a) and (b), μSOFC is found to yield better performance when isothermal conditions are applied. This is because the comparable high cell temperatures under adiabatic conditions contribute to a lower reversible voltage, thus deteriorating the output capacity of μSOFC. From Fig. 5(c), the mean cell temperature is maintained at 1076 K under isothermal conditions, whereas the temperature soars over 1200 K under adiabatic conditions. As the current density increases, the mean cell temperature is augmented drastically and the reduction in reversible voltage becomes more prominent, leading to a lower power output. From Fig. 5(b), the maximum power density is 0.19 W cm^{-2} at 0.35 A cm^{-2} for adiabatic conditions, compared to 0.32 W cm^{-2} at 0.67 A cm^{-2} for isothermal conditions. The enormous rise in mean cell temperature under adiabatic conditions also reveals the ineffectiveness of heat convection by the flowing reactants. Similar to the conclusion drawn by Srikar et al. [6], we find that thermal energy produced by the electrochemical reaction primarily dissipates through in-plane heat conduction inside the μSOFC.

Fig. 6 shows the temperature distribution at the anode/electrolyte interface under adiabatic conditions for a voltage of 0.18 V. As depicted in Fig. 6, there exist tremendous temperature gradients near the reactant inlets for all flow channel designs. The temperature deviations in μSOFC are so great (approximately 350–400 K) under adiabatic conditions that thermal stresses may jeopardize the reliability of the microstructure. This proves that appropriate thermal management is vital to both electrochemical performance and structural stability for μSOFC. Moreover, the optimization of packaging near the inlet regions is of particular importance to minimizing the incidence of cracks.

The increase of mean cell temperature under adiabatic conditions also causes other interesting effects. Fig. 7 presents the varying pressure drops between inlet and outlet of the serpentine flow channel design with current density under different thermal boundary conditions. In the anode channel, the pressure drop increases with current density regardless of thermal boundary conditions. From stoichiometry, consuming 1 kg of hydrogen results in generating 18 kg of steam. Hence, a larger pressure drop is required to discharge the excess steam when an electrochemical reaction takes place. As current density increases, more steam is produced and the pressure drop is augmented accordingly. Yet even when current density is equivalent, the pressure drop in the anode channel under adiabatic conditions is higher than that under isothermal conditions. This is ascribed to the increase in viscosity and reduction in density for gases at enhanced cell temperature under adiabatic conditions. In the cathode channel, however, the

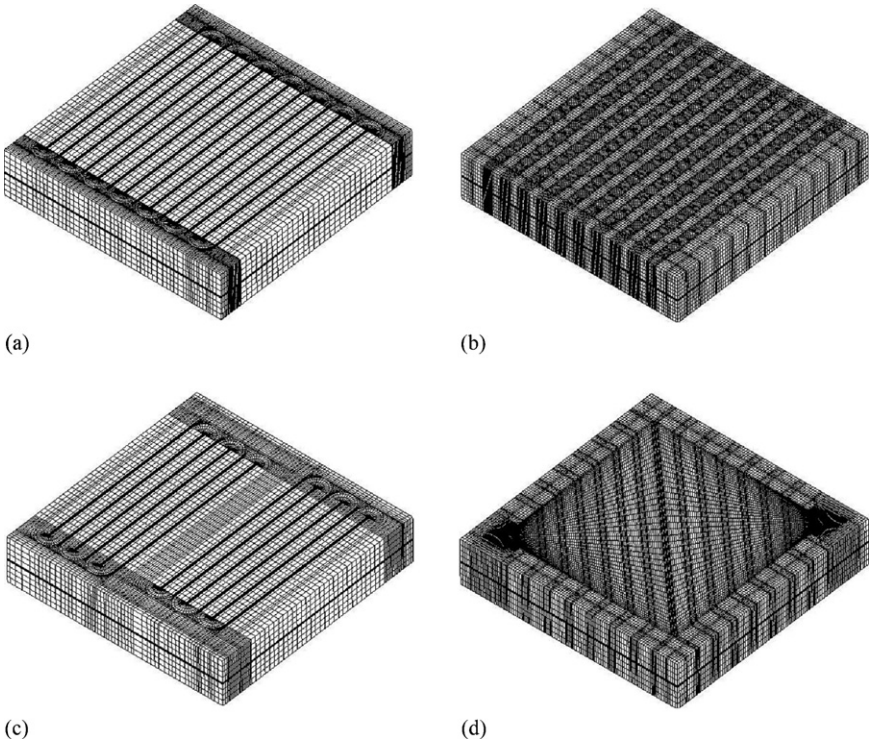

Fig. 4. Schematic drawing of the grids for (a) serpentine, (b) rod bundle, (c) double serpentine and (d) oblique rib.

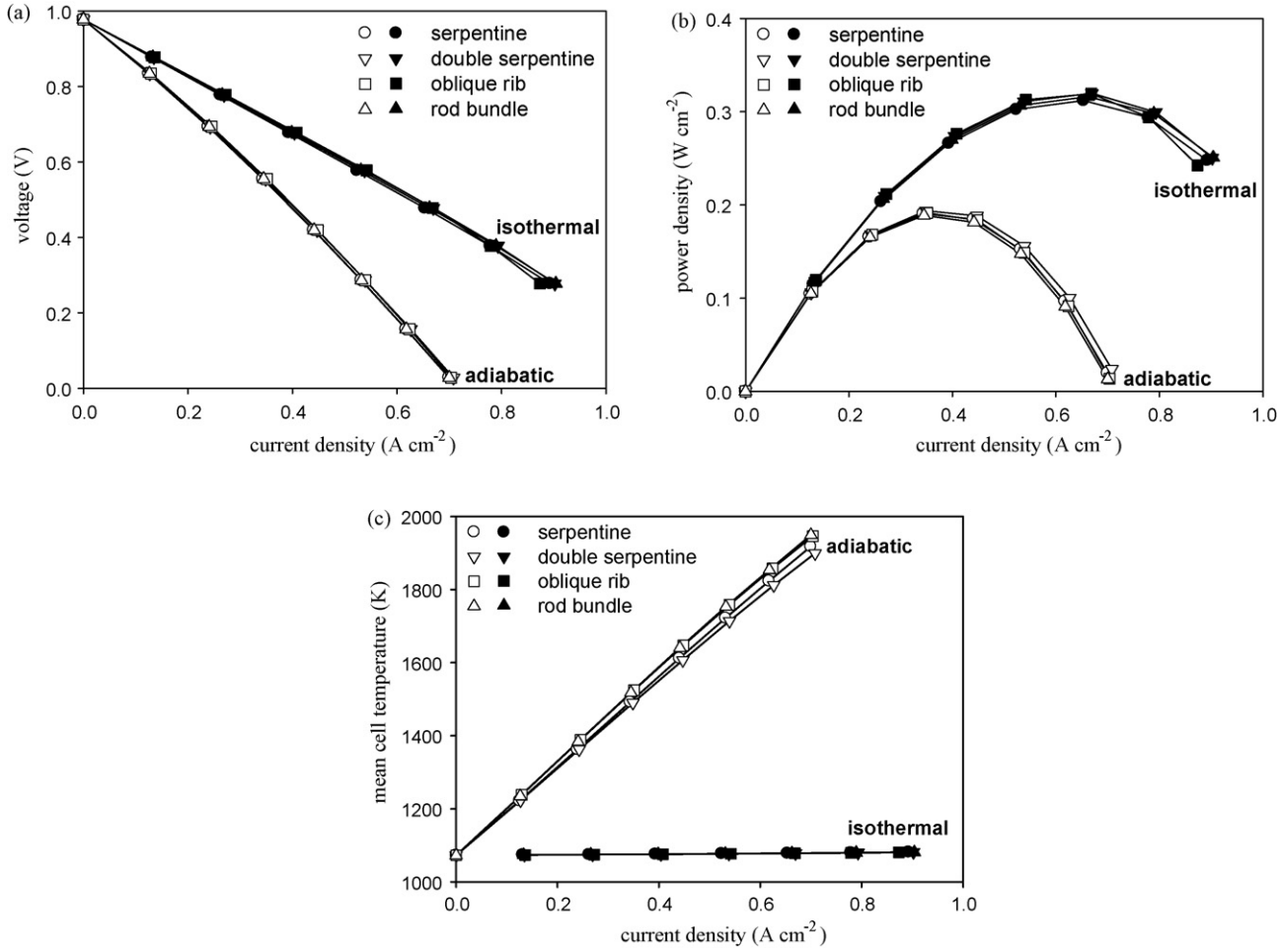

Fig. 5. Comparison of adiabatic and isothermal boundary conditions, pure oxygen is used: (a) voltage vs. current density; (b) power density vs. current density; (c) mean cell temperature vs. current density.

variations in pressure drop with current density exhibit opposite trends for different thermal boundary conditions. Since there is no substance produced by the cathode reaction, pressure drop is diminished with an increase in current density under isothermal conditions. In contrast, the effects of the temperature-dependent physical properties become greater than oxygen exhaustion due to the immense increase in cell temperature under adiabatic conditions. As a result, pressure drops increases slightly with increasing current density when adiabatic conditions are imposed.

To reduce the operating temperature of μSOFC under adiabatic condition, there are two approaches to improve the convection effects: increasing the flow rate of oxidant and increasing the temperature difference of reactants between inlets and outlets. While large temperature gradient induces undesirable thermal stress, increasing the flow rate of oxidant is the more viable option. To ensure thermal balance, the heat production rate of the cell should be equivalent to the heat transfer rate by convection:

$$i_{\mathrm{av}}\left(-\sum_i \frac{a_i' h_i}{M_i} - E\right) = \sum_i \dot{m}_i c_{\mathrm{p},i}(T_{\mathrm{outlet},i} - T_{\mathrm{inlet},i}) \tag{9}$$

where $-\sum_i a' h_i/M_i$ and E represent the thermoneutral voltage and the operating voltage, respectively. To allow μSOFC to operate below 1200 K, the temperature difference $T_{\mathrm{outlet},i} - T_{\mathrm{inlet},i}$ is assumed to be less than 100 K. From Eq. (9), the required mass flow rate of oxygen is then plotted against current density in Fig. 8. Since heat is produced at higher rate as current density increases, larger mass flow rate of oxygen is demanded to achieve thermal balance. Due to the low specific heat of oxygen, the required mass flow rate is nearly two orders of magnitude higher than the stoichiometric value at a current density of 0.7 A cm^{-2}.

3.2. Influences of oxygen composition

Fig. 9 depicts the cell characteristics obtained under isothermal condition with different oxidant compositions. Even stoichiometry is retained, less current density is delivered with the 50% O_2/50% N_2 composition as depicted in Fig. 9(a). For the present μSOFC model, the Péclet number is in the order of 1, indicating that local diffusion dominates over bulk advection [11]. When pure oxygen is used, oxidant is migrated to the cathode surface so efficiently that no diffusion limitation occurs. On the contrary, oxygen molecules have to diffuse through nitrogen to reach the cathode surface with lower oxygen compositions. For the serpentine design under isothermal condition, Fig. 9(c) and (d) shows the variations of hydrogen and oxidant utilization rates with the operating voltage. From Fig. 9(c) and (d), using the 50% O_2/50% N_2 composition results in reduction of both hydrogen and oxidant utilization rates. Hence, the cathode performance is affected by gas diffusion pronouncedly and output power experiences 16–23% decrease. For air, the output power of μSOFC is not only affected by diffusion limitation but also by the supplying rate of oxidant. Since the mass flow rate of air is fixed at 8×10^{-8} kg s^{-1}, the oxidant utilization rate is close to 100% when

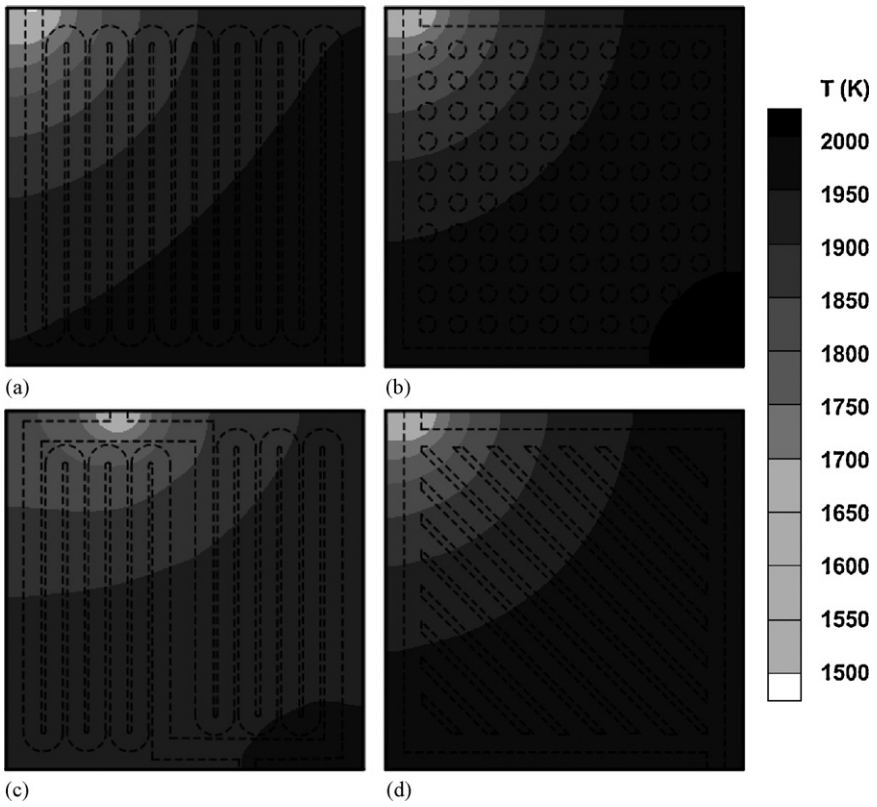

Fig. 6. Temperature profiles at the anode/electrolyte interface under adiabatic conditions, $E = 0.18$ V, $z = 1.25$ mm: (a) serpentine, (b) rod bundle, (c) double serpentine and (d) oblique rib.

the operating voltage is below 0.4 V. Although only 24% of hydrogen is consumed, the cell is already starved of oxidant. Comparing to pure oxygen, the output power of using air is decreased 90–92% as shown in Fig. 9(b). For both air and the 50% O_2/50% N_2 composition, the deterioration of performance is most noticeable when the flow channel design is oblique rib. More details of the effects of flow channel design are discussed in Section 3.3.

Besides poorer performance, using lower oxygen compositions has other downsides. To prevent the depletion of oxygen at cathode, mass flow rate is required to increase for lower oxygen composition and pressure drop is augmented consequently. Hence, costs of delivering oxidants are increased and the risk of fuel crossover is heightened. These problems become more severe when the oxidant contains less oxygen.

Another potential issue with using an oxidant of lower oxygen composition lies in the preheating process. Since SOFC is designated to operate at high temperatures, it is necessary to heat the reactants before entering the cell. The total power required to preheat the reactants $\dot{W}_{\text{preheat}}$ can be calculated by Eq. (10):

$$\dot{W}_{\text{preheat}} = \sum_i \dot{m}_i [h_i(1073\,\text{K}) - h_i(300\,\text{K})] \tag{10}$$

By supplying the 50% O_2/50% N_2 composition, 0.06 W more power are necessary to raise the reactants to 1073 K, as compared to

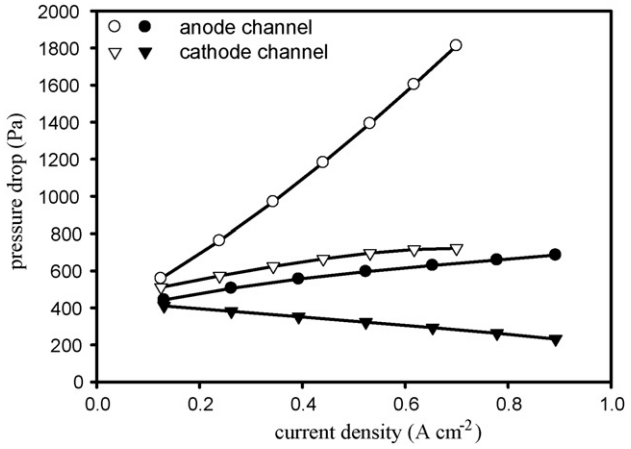

Fig. 7. Pressure drops in anode and cathode channels vs. current density for serpentine design. Solid symbols represent isothermal conditions, while open symbols represent adiabatic conditions.

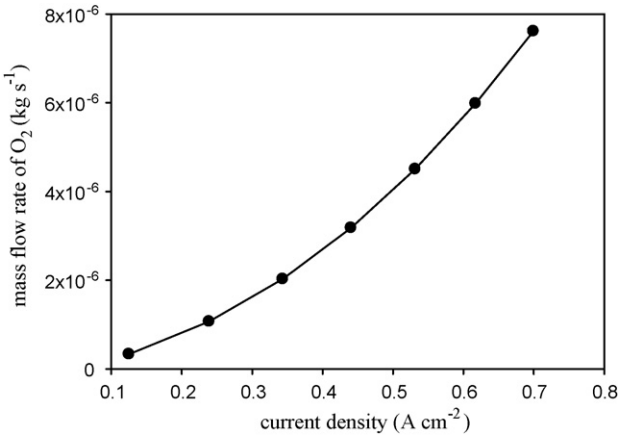

Fig. 8. To keep the cell temperature below 1173 K under adiabatic condition, the estimated mass flow rate of oxygen vs. current density. Mass flow rate of hydrogen is fixed at 10^{-8} kg s^{-1}.

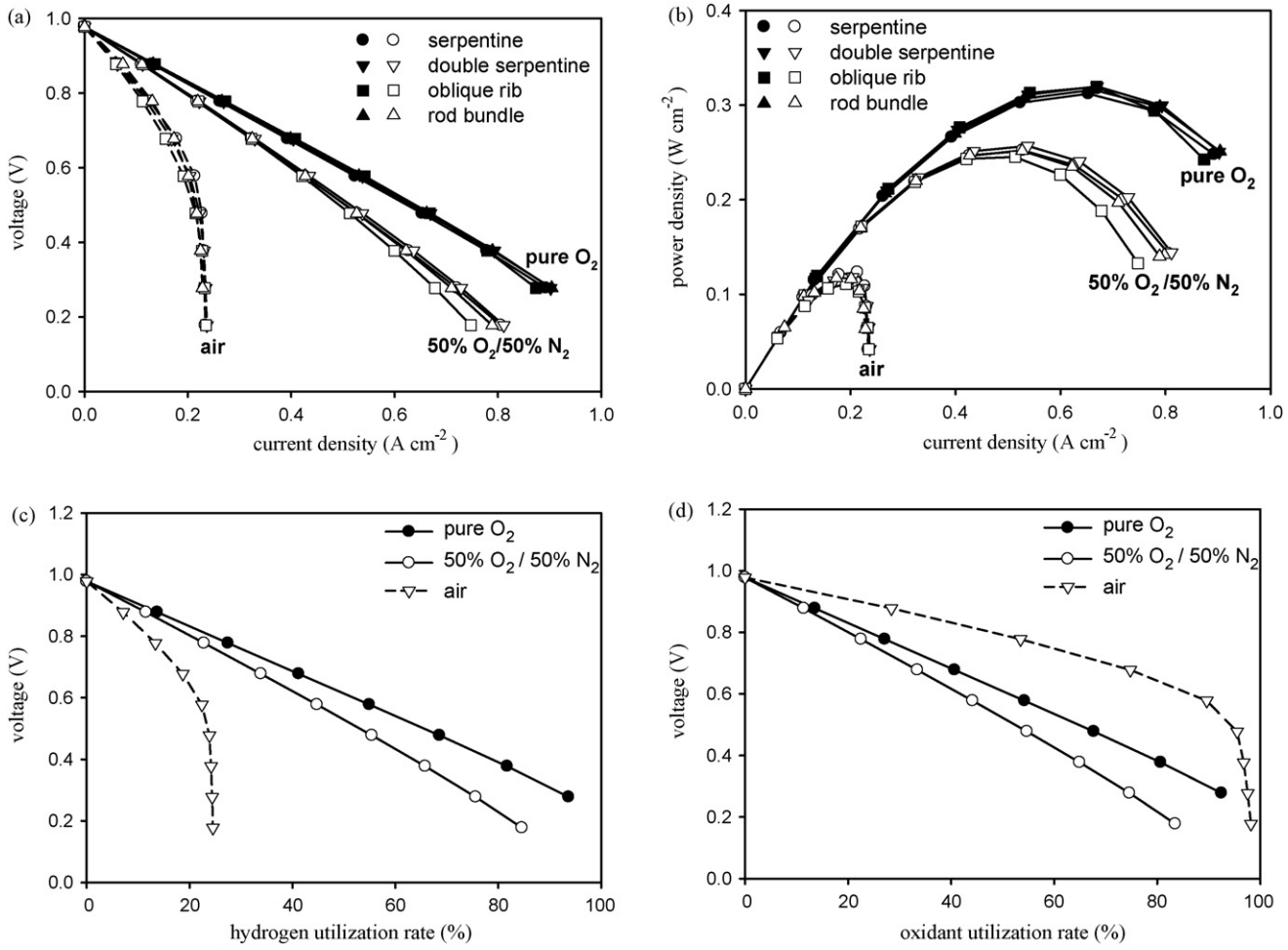

Fig. 9. Comparison of using different oxygen composition under isothermal conditions: (a) voltage vs. current density; (b) power density vs. current density; (c) voltage vs. hydrogen utilization rate for various oxygen compositions. Isothermal condition, serpentine flow channel design (d) voltage vs. oxygen utilization rate for various oxygen compositions. Isothermal condition, serpentine flow channel design.

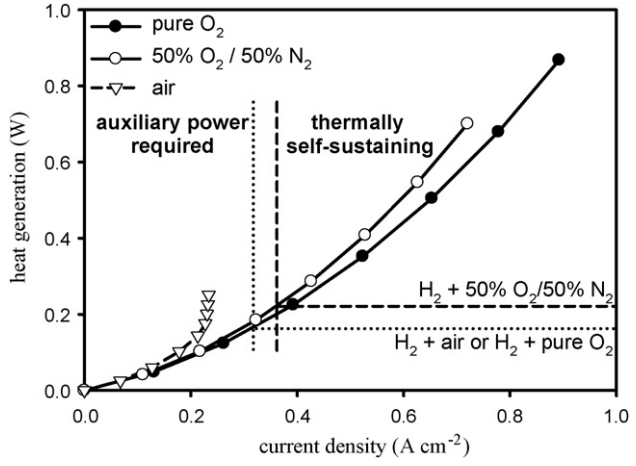

Fig. 10. Heat generation vs. current density for serpentine design under isothermal conditions.

pure oxygen. This supplementary need drains nearly all the power output μSOFC can supply, suggesting that implementing a heat recuperation configuration is essential to μSOFC. Using the equation suggested by Larminie and Dicks [12], Fig. 10 shows the variation of heat generated by μSOFC operation with current density for the serpentine design using different oxidant compositions. The horizontal dashed lines denote the heat absorption rates required to preheat hydrogen and oxidants from room temperature to 1073 K. For pure oxygen and the 50% O_2/50% N_2 composition, the recovered enthalpy is sufficient to preheat the reactants at moderate to high current density if the exothermic nature of the electrochemical reaction is employed. However, an auxiliary heating system is still needed at low current densities, such as during the start-up. By using the 50% O_2/50% N_2 composition, the minimum current density needed for thermal self-sufficiency is 0.36 A cm^{-2}, slightly higher than when using pure oxygen because additional energy is required to warm up the excess nitrogen. In contrast, μSOFC can never be thermally self-sustaining by using air and auxiliary heating system becomes essential regardless of current densities. Although air is commonly used in macroscale systems, oxidant with higher oxygen composition is more feasible for μSOFC.

3.3. Influences of flow channel designs

From Fig. 9, flow channel design demonstrates no apparent influences on the performance of μSOFC when using pure oxygen. Since oxygen is abundant and cell temperatures are high, both activation overpotential and concentration overpotential become

insignificant. As a result, voltage decreases linearly with increasing current density, suggesting a strong dominance of ohmic overpotential in μSOFC. When the oxygen content decreases, performance distinctions become recognizable. As indicated in Section 3.2, output power for the oblique rib design is 3.2–18% lower than for other flow channel designs at moderate to high current densities when the lower oxygen composition is used.

Activation, ohmic, and concentration overpotentials are calculated to estimate their individual contributions to the overall losses. Instead of using the simplified linear current–potential relation or the Tafel equation, the Bulter–Volmer equation is solved iteratively for a given current density to determine activation overpotential [13]. Once ohmic overpotential is evaluated by Ohm's Law, concentration overpotential is obtained by subtracting activation and ohmic overpotentials from the overall losses. For the 50% O_2/50% N_2 composition under isothermal condition, the contributions of different overpotential to the overall losses are depicted in Fig. 11. At a given current density, activation and ohmic overpotential are nearly identical for all flow channel designs. Because a consistent contact area of interconnects and electrodes is maintained, the performance deficiency is mainly ascribed to the poor dispersion of species in the interconnect. From Fig. 11, it is found that activation, ohmic, and concentration overpotentials present 25, 56, and 19%, respectively, of the overall losses for the oblique rib design at an operating voltage of 0.28 V.

Fig. 12 illustrates the mass fraction of oxygen at the cathode/electrolyte interface for various flow channel designs using 50% O_2/50% N_2 under isothermal condition. For the serpentine and double serpentine designs, oxygen content is reduced gradually along the flow channel due to the electrochemical reaction. For the rod bundle design, oxygen content decreases radially from the inlet region. Mass fractions of oxygen for the aforementioned designs

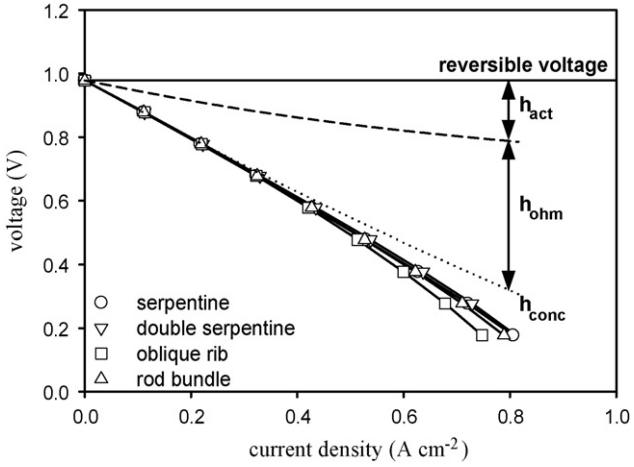

Fig. 11. Contributions of activation, ohmic, and concentration overpotential to the overall losses. Isothermal condition, the 50% O_2/50% N_2 composition is used.

generally remain above 0.2–0.3 in most active areas. On the contrary, the configuration of the oblique rib design favors oxidant flow in the inlet–outlet diagonal direction. With limited cross-rib diffusion, oxygen depletion is observed adjacent to the two opposite corners. Mass fractions of oxygen are found to fall below 0.15 in these 'dead zones' for the oblique rib design, resulting in poorer performance.

To further analyze the overall performance, pressure drops associated with fuel delivery are taken into consideration. Fig. 13 exhibits the pressure drops in cathode channels for various flow channel designs using the 50% O_2/50% N_2 composition. For the serpentine design, the configuration of a long single duct evokes a

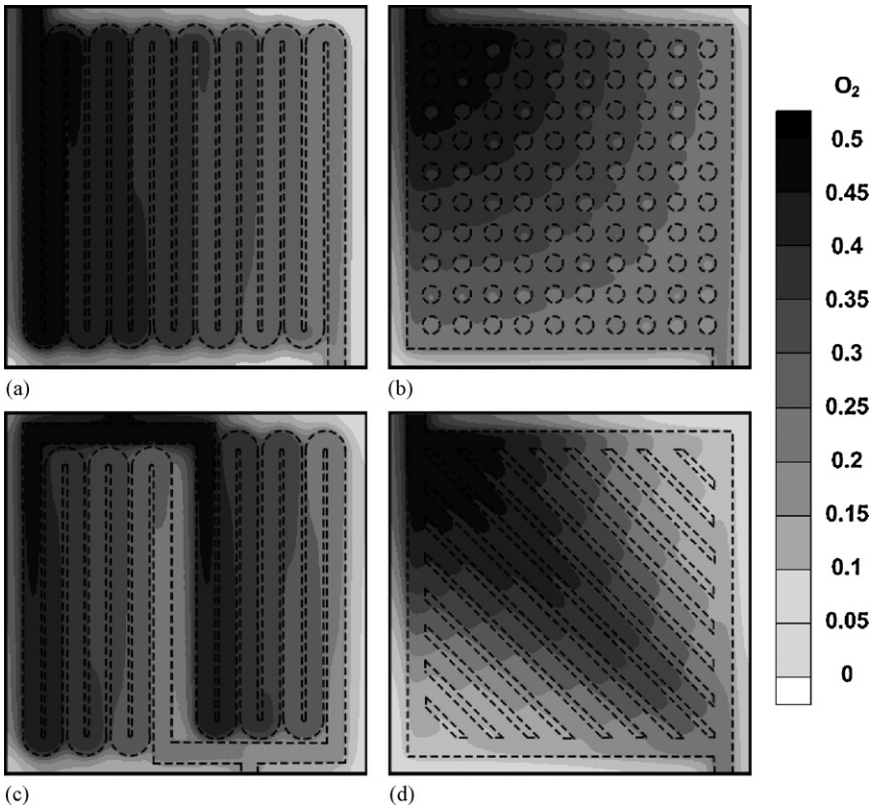

Fig. 12. Oxygen mass fraction at the cathode/electrolyte interface under isothermal conditions, E = 0.18 V, z = 1.05 mm: (a) serpentine, (b) rod bundle, (c) double serpentine and (d) oblique rib.

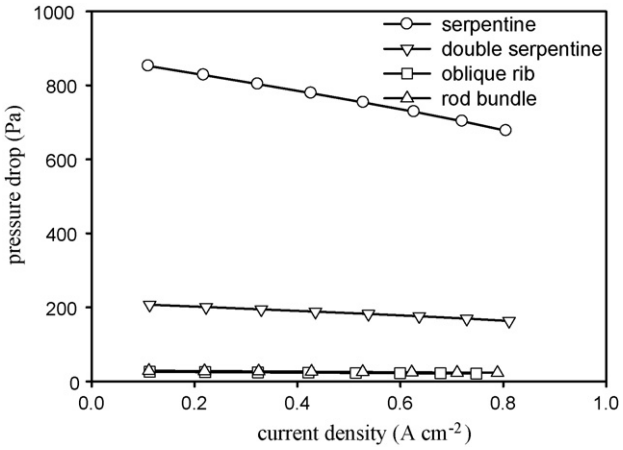

Fig. 13. Pressure drop in cathode channel vs. current density for various flow channel designs. Isothermal condition, the 50% O_2/50% N_2 composition is used.

high-pressure drop varying from 677 to 852 Pa. Despite that similar results are observed for the double serpentine design, the pressure drop in the double serpentine design is smaller than for the serpentine design due to branching, ranging from 163 to 207 Pa. For both the oblique rib and rod bundle designs, pressure drops are significantly diminished. Since flow resistances are very small, pressure drops between inlets and outlets are nearly negligible (<30 Pa). The minimum power required to stream the reactants $\dot{W}_{\text{flow}}$ can be determined by

$$\dot{W}_{\text{flow}} = \sum_i \frac{\Delta P_i \dot{m}_i}{\rho_i} \tag{11}$$

From Eq. (11), a larger pressure drop results in greater power consumption required to deliver the fuels for one flow channel design. Although more power is spent by the compressor to overcome the wall friction for the serpentine design, $\dot{W}_{\text{flow}}$ only takes up less than 1% of the total power output due to the low flow rates in μSOFC. Consequently, the expenditure of auxiliary electricity for fuel delivery is insignificant in μSOFC.

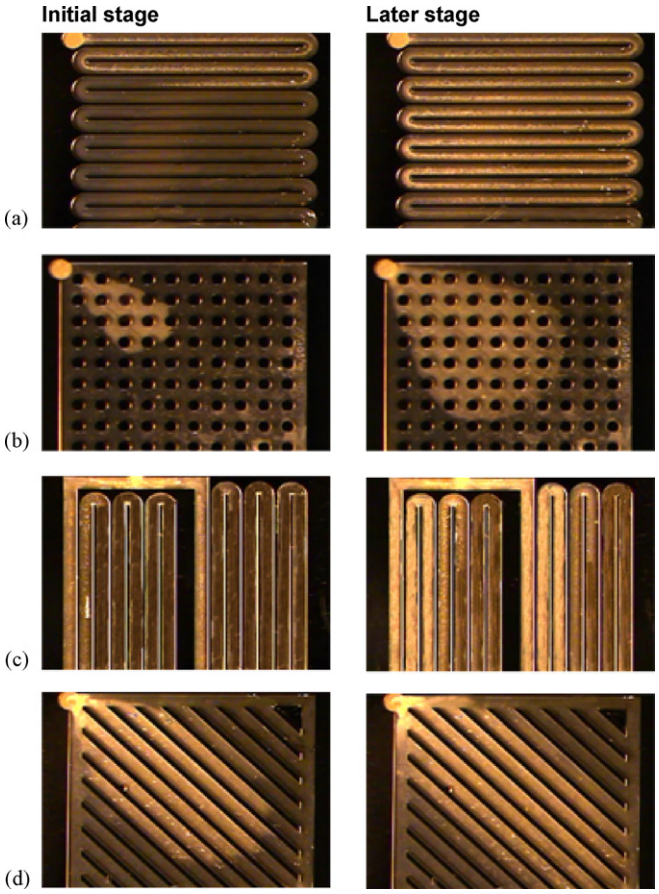

Fig. 15. Flow visualization insides different flow channel designs: (a) serpentine, (b) rod bundle, (c) double serpentine and (d) oblique rib.

4. Flow visualization

Surface marking technique [14] is employed to observe the gas flow in various flow channel designs of μSOFC. The prototypes of

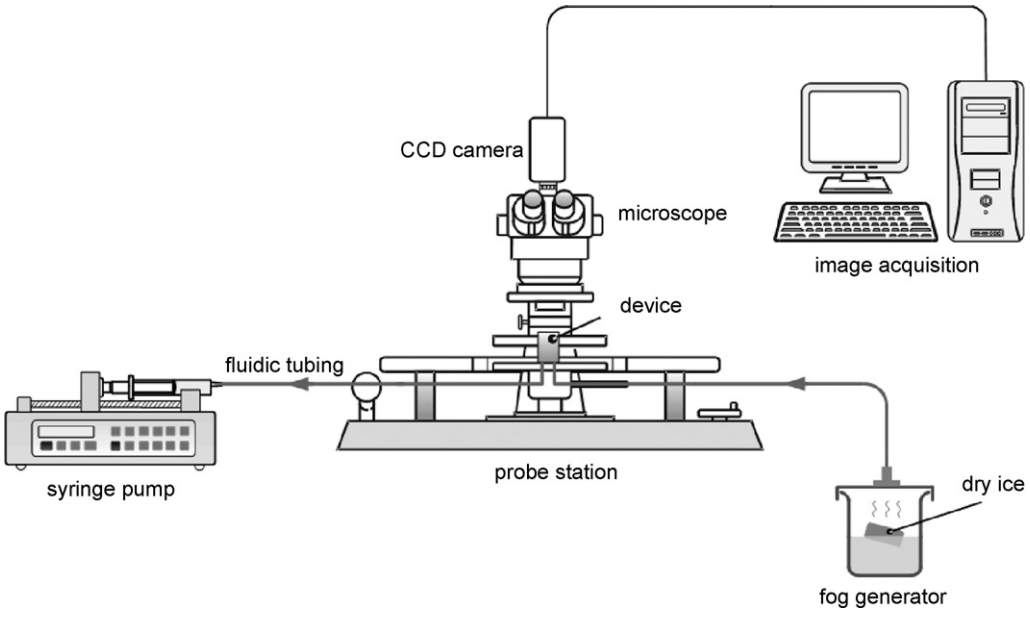

Fig. 14. Experimental setup for flow visualization.

the four flow channel designs are fabricated by micromachining technologies on a silicon wafer. A two-step deep reactive ion etching (DRIE) process is facilitated to define the microchannels and through-wafer fluidic ports. Before dicing, the silicon wafer is anodically bonded to a Pyrex glass substrate to allow flow visualization. The experimental setup for flow visualization is depicted in Fig. 14. As shown in Fig. 14, dry ice and water are placed in a beaker to create dense clouds of fog. The white fog is then streamed into the microchannel by a syringe pump. The flow rate is set to 2 ml min^{-1} so that the corresponding Reynolds number is within the same range as the numerical simulations. Due to the extreme cold, liquid fog droplets freeze to the microchannel's surface, forming white frost to qualitatively map flow distributions. Under the ring fluorescent illumination, image sequences are recorded by a 30 fps CCD camera with a resolution of 768×494 pixels (jai CV-S3300). The results are displayed in Fig. 15 for the four flow channel designs. For both the serpentine and double serpentine designs, we find that the growth of the white frost propagates progressively along the flow channel. For the diagonal rib design, white frost tends to disperse along the diagonal direction, resulting in the appearance of "dead zones" in the vicinity of the two opposite corners. For the rod bundle design, white frost disperses from the inlet and spreads more widely during the transport process. The front resumes a round shape that resembles the circular iso-concentration lines predicted by the numerical simulation. Although these surface patterns are subject to the combined influences of flow, pressure, heat, and mass transfer, the surface marking technique successfully reveals the low transport regions in the flow channel and can serve as a useful tool for designing interconnects of μSOFC in the future.

5. Conclusions

This study presents the results from the cell-level simulation of microscale SOFC. The impacts of thermal operating conditions, oxidant compositions, and flow channel designs are investigated. Among these three parameters, thermal operating conditions are found to play a critical role in the performance of μSOFC. Under adiabatic conditions, the cell temperature is much higher than that under isothermal conditions such that the tremendous decrease of reversible voltage results in poorer cell performance. Moreover, the advection effect is so weak that the mass flow rate of oxygen is required to increase tremendously to keep the cell operating below 1200 K. The primary heat transfer mechanism in μSOFC is conduction, which suggests that proper packaging for μSOFC is vital to maintaining an isothermal operating environment and achieving maximum output power.

For μSOFC, concentration overpotential is less significant than ohmic overpotential. Nevertheless, oxidant composition exerts substantial effects on μSOFC's performance. When the 50% O_2/50% N_2 composition is used, output power experiences a 16–23% reduction compared to that of pure oxygen. This is because local diffusion dominates the species transport in microscale and diffusion limitations occur with the presence of nitrogen. The effects of diffusion limitations are particularly evident for the oblique rib design. Lacking effective cross-channel transport, 'dead zones' occur in the oblique rib design and as a result performance is deteriorated at moderate to high current densities. The presence of 'dead zones' is verified by the results of flow visualization. The surface marking technique used in this study provides a valuable insight into the impacts of mass transport in μSOFC.

The dominance of local diffusion over advection also offers a plausible explanation of the modest influences of flow channel designs in our study. Due to the small Péclet number, species distribute uniformly as long as the diffusion length is larger than the feature size [15]. Hence, the variations in output power are less than 10% among the four flow channel designs even when air is used. To examine the feasibility of μSOFC, power consumed by fuel preheating and delivery is explored. It is found that the power required to supply the fuel to the cell only occupies less than 1% of total output power. Yet, power utilized to preheat fuels would rigorously attenuate the output capacity. Therefore, it is essential to implement a heat recuperation configuration for μSOFC. A potential solution is recycling the waste heat from the electrochemical reaction to preheat fuels. For current densities larger than 0.36 A cm^{-2}, the recovered heat should be adequate to sustain thermal self-sufficiency when the 50% O_2/50% N_2 composition or pure oxygen is supplied. On the other hand, using air in μSOFC is never thermally self-sustaining and auxiliary preheating system is always in need. As a result, employing oxidant with higher oxygen composition is vital for the success of μSOFC.

Acknowledgment

This work is supported by the National Science Council of Taiwan under grant nos. NSC 93-2623-7-011-006-ET and NSC 94-ET-7-011-006-ET.

References

[1] K. Fu, A.J. Knobloch, F.C. Martinez, D.C. Walther, A.C. Fernandez-Pello, A.P. Pisano, D. Liepmann, Design and fabrication of a silicon-based MEMS rotary engine, in: Proceedings of ASME International Mechanical Engineering Congress and Exposition, New York, 2001.
[2] W. van der Wijngaart, A. Berrier, G. Stemme, Sensors and Actuators A: Physical 100 (2002) 77–83.
[3] A.F. Jankowski, J.P. Hayes, R.T. Graff, J.D. Morse, Micro-fabricated thin-film fuel cells for portable power requirements, in: R.B. Schwarz, G. Ceder, S.A. Ringel (Eds.), Proceedings of Materials Research Society Symposium, San Francisco, CA, 2002, pp. 93–98.
[4] F. Issacci, Thermal management and transport phenomena in fuel cell system—practical issues, in: Proceedings of the 6th ASME-JSME Thermal Engineering Joint Conference, Torrance, CA, 2003.
[5] J.D. Morse, A.F. Jankowski, A novel thin film solid oxide fuel cell for microscale energy conversion, in: Proceedings of ASME International Mechanical Engineering Congress and Exposition, Nashville, Tennessee, 1999.
[6] V.T. Srikar, K.T. Turner, T.Y.A. Ie, S.M. Spearing, Journal of Power Sources 125 (2004) 62–69.
[7] Y. Tang, K. Stanley, J. Wu, D. Ghosh, J. Zhang, Journal of Micromechanics and Microengineering 15 (2005) S185–S192.
[8] Z. Shao, S.M. Haile, J. Ahn, P.D. Ronney, Z. Zhan, S.A. Barnett, Nature 435 (2005) 795–798.
[9] CFD-ACE+ V2003 User Manual, CFD Research Corporation, Huntsville, Alabama, 2003.
[10] P.A. Ramakrishna, S. Yang, C.H. Sohn, Journal of Power Sources 158 (2006) 378–384.
[11] N.-T. Nguyen, Z. Wu, Journal of Micromechanics and Microengineering 15 (2005) R1–R16.
[12] J. Larmine, A. Dicks, Fuel Cell Systems Explained, first ed., John Wiley & Sons, West Sussex, 2000.
[13] S.H. Chan, K.A. Khor, Z.T. Xia, Journal of Power Sources 93 (2001) 130–140.
[14] S. Tavoularis, Measurement in Fluid Mechanics, Cambridge University Press, Cambridge, United Kingdom, 2005.
[15] Z. Lin, J.W. Stevenson, M.A. Khaleel, Journal of Power Sources 117 (2003) 92–97.